PAPER

Check for updates

Harnessing the kinetics of $LiMn_{0.5}Fe_{0.5}PO_4$ in energy-dense layered-olivine blend cathodes for lithium-ion batteries

Seamus Ober and Arumugam Manthiram [ID] *

Layered-olivine blends have been a topic of recent commercial and research interest due to their thermal stability, cycling stability, and low cost, but the low energy density of olivine cathodes remains a key challenge. Despite the low theoretical energy density of olivine cathodes, the practical energy density of layered-olivine blend cathodes depends strongly on the operating conditions. Herein, we explore how the performance of blends of Nb-incorporated $LiNi_{0.8}Mn_{0.1}Co_{0.1}O_2$ (Nb@NMC811) and $LiMn_{0.5}Fe_{0.5}PO_4$ (LMFP) depends on various operating conditions. With the help of a novel technique for rapidly comparing the energy density of cathodes for different operating conditions, it is found that the layered-olivine blends offer the most competitive energy density during high-rate, high-temperature, and low state-of-charge (SOC) operations. This observation is ascribed primarily to the redox buffer effect of the $Fe^{2+/3+}$ couple, which offers more facile Li^+ transport kinetics than layered oxides at low operating voltages (<3.6 V $vs.$ Li/Li^+). Under high electrode loading conditions in full-cells, it is demonstrated that the layered-olivine blends can offer more competitive energy density compared to pure Nb@NMC811 with appropriate C-rate and temperature conditions. These findings reveal how operating conditions can further improve the cost benefit of layered-olivine blends.

Broader context

Lithium-ion batteries (LIBs) are critical to meet the demands of the world's growing technological landscape. As attention shifts toward large-scale LIB applications, such as electric vehicles, the need for energy-dense, low-cost, and safe LIBs is increasingly stringent. Unfortunately, the most energy-dense cathode materials—high-nickel layered oxides—are also expensive and subject to safety concerns. By blending in olivine-phase cathode materials, which exhibit low cost and excellent stability, the cost and safety can be improved. However, this blending approach also sacrifices the energy density of the cathode, imposing a tradeoff in performance metrics. Herein, we explore the relationships between electrochemical kinetics and operating conditions for layered-olivine cathode blends. We identify how certain operating conditions, such as elevated temperature and high discharge rate, can minimize the energy density loss incurred by blending olivine-phase cathodes into high-nickel layered oxides. Ultimately, this work provides direction for the development and application of layered-olivine blended cathodes to maximize their cost benefit.

Introduction

Lithium-ion batteries (LIBs) have proven themselves a vital technology in the modern era, powering a diverse range of products ranging in scale from wearable electronics to massive grid-storage battery systems. Each technological application of lithium-ion batteries demands a unique balance between volumetric energy density, power density, cost, longevity, and other metrics. The ability of a battery to meet these demands is determined largely by its cathode chemistry. Thus, a variety of different cathode materials have been developed, each offering a unique set of advantages.[1,2]

Blended cathode materials, typically consisting of physical mixtures of two distinct cathode materials, have been widely explored and implemented as an approach to combine the advantages of each constituent material.[3–5] The two most widely commercialized classes of cathode materials are layered oxides ($LiMO_2$, M = Ni, Mn, Co, *etc.*) and olivines ($LiMPO_4$, M = Fe, Mn).[6–9] Layered oxides offer competitive energy density (*e.g.*, ~700–750 W h kg^{-1} for $LiNi_{0.8}Mn_{0.1}Co_{0.1}O_2$), but rely on costly materials and present safety concerns due to their poor thermal stability. Moreover, cycling to high cutoff charge voltages aggravates their thermal instability and accelerates parasitic side reactions, leading to irreversible capacity loss.[10–12]

Materials Science and Engineering Program and Texas Materials Institute, The University of Texas at Austin, Austin, Texas 78712, USA.
E-mail: manth@austin.utexas.edu

In contrast, olivine cathodes generally offer excellent cycling stability, safety, and low cost. However, their theoretical energy density is lower than that of layered oxides, and their practical energy density (e.g., ~500–600 W h kg^{-1} for LiMn$_x$Fe$_{1-x}$PO$_4$)[13] is further reduced by the requirement for nanosizing and carbon-coating to compensate for low electronic conductivity.[14,15]

Increasing substitution of Mn for Fe significantly improves the theoretical energy density of the olivine cathode due to the high Mn$^{2+/3+}$ redox voltage. However, as identified by previous work, this strategy also introduces several challenges. Mn^{3+} exhibits Jahn–Teller distortion, leading to anisotropic lattice contraction, which results in sluggish Mn$^{2+/3+}$ redox kinetics.[15,16] Additionally, the tendency of Mn to dissolve into the electrolyte, particularly under high temperature and state-of-charge (SOC) conditions, raises concerns related to crossover effects and capacity fade.[17,18] These effects, in combination with low tap/press density, limit the practically achievable energy density, stability, and rate capability of LiMn$_x$Fe$_{1-x}$PO$_4$ cathodes.[16,19] Additionally, the step in the voltage profile of LiMn$_x$Fe$_{1-x}$PO$_4$, stemming from the different operating voltages of the Mn$^{2+/3+}$ and Fe$^{2+/3+}$ redox couples, renders it unsuitable as a standalone cathode; nevertheless, it is an excellent candidate for blending with other materials.[20] Thus, the complementary advantages of these two cathodes make them particularly attractive candidates for blending, as has been demonstrated by research interest[21,22] and commercialization of layered-olivine blends.

Recently, our group demonstrated that blending LiMn$_{0.5}$Fe$_{0.5}$PO$_4$ into layered oxides is a more effective strategy for reducing cost ($ kW^{-1} h^{-1}) than raising the voltage cutoff or adjusting the composition of the layered oxide constituent of the cathode.[21] Other studies have explored a method for combining a layered cathode with smaller particle size LiFePO$_4$ to achieve similar volumetric energy density.[23] Generally, however, when blending olivines into layered oxides, the material energy density (Wh kg^{-1}, Wh L^{-1}) is compromised somewhat for more favorable cost ($ kW^{-1} h^{-1}), electrochemical stability,[13,24] and thermal stability.[25,26]

Although previous studies have addressed various characteristics of layered-olivine blends, the impacts of various operating conditions on their behavior have yet to be comprehensively investigated. Due to the unique properties of each cathode material, effects arising due to differences in redox kinetics and voltages are expected to play significant roles in the kinetic behaviors of layered-olivine blends. To thoroughly address the behavior of this class of blended cathodes and set sensible cathode design parameters, it is critical to consider the rate, SOC/voltage, and temperature conditions under which the battery is expected to operate.

In this work, we investigate a layered-olivine blended cathode consisting of Nb—coated LiNi$_{0.8}$Mn$_{0.1}$Co$_{0.1}$O$_2$ (Nb@NMC811) and doped, carbon-coated LiMn$_{0.5}$Fe$_{0.5}$PO$_4$ (LMFP) as a model cathode system to balance the demands of high energy density, safety, low cost, and high rate capability. We develop, validate, and apply a novel critical rate analysis

(CRA) technique to predict the operating conditions under which blending the LMFP into Nb@NMC811 is most beneficial for energy density and cycle life. We show that due the buffer effect of Fe$^{2+/3+}$ redox in LMFP, it is possible for layered-olivine blends to deliver higher energy density than their layered oxide counterparts at low states of charge (SOC). More generally, we address how certain design and operating conditions can be selected to exploit this phenomenon, minimizing the energy density penalty incurred during high-SOC operations. Ultimately, this understanding can be used to maximize the cost benefit of layered-olivine blends to achieve low-cost and energy-dense cathodes.

Experimental section

Materials synthesis

LiNi$_{0.8}$Mn$_{0.1}$Co$_{0.1}$O$_2$ (NMC811) was synthesized from a Ni$_{0.8}$Mn$_{0.1}$Co$_{0.1}$(OH)$_2$ precursor. This precursor was synthesized by hydroxide coprecipitation, as described previously. In brief, an aqueous solution of NiSO$_4$·6H$_2$O (Chemsavers), MnSO$_4$·H$_2$O (Thermo Scientific), and CoSO$_4$·7H$_2$O (Alfa Aesar) and a separate solution of KOH in deionized water were pumped at controlled rates into a reaction solution containing NH$_4$OH (Fisher Chemical) as a chelating agent. The reaction solution was maintained at 50 °C and pH = 11.50. The product was recovered by filtration and washed several times with deionized water before transferring to a 110 °C oven for storage. After drying for several days, the powder was mixed with preground LiOH·H$_2$O in 5 mol% excess. This mixture was then calcined under O$_2$ atmosphere at 770 °C for 12 h to yield NMC811. To add a Nb coating, ammonium niobium oxalate (ANO, CBMM) equivalent to 0.50 mol% was dissolved in ~0.50 mL of methanol, which was then added to 2.0 g dry NMC811 powder. This mixture was stirred at 1000 rpm for 3 minutes with a Thinky ARV-310 mixer, after which the powder was observed to be saturated with minimal excess methanol. The powder was then placed in a 110 °C vacuum oven for 2 h to evaporate the methanol, after which the powder was observed to have uniform appearance with no niobium-rich regions. Finally, the powder was mixed with additional preground LiOH·H$_2$O (~15 mg) and heated at 770 °C under O$_2$ atmosphere to form the LiNbO$_3$ coating.

LiMn$_{0.5}$Fe$_{0.5}$PO$_4$ (LMFP) was synthesized by a multi-step synthesis described in our group's previous work as P-LMFP.[16] First, NH$_4$Mn$_{0.5}$Fe$_{0.5}$PO$_4$·H$_2$O was prepared by coprecipitation. A metal solution was prepared containing 0.50 M FeSO$_4$·7H$_2$O (Thermo scientific), 0.50 M MnSO$_4$·H$_2$O (Thermo scientific), and 1.0 M H$_3$PO$_4$ (Sigma-Aldrich) dissolved in 250 mL deionized water, with 0.18 g ascorbic acid to inhibit oxidation of the transition metals. A base solution was prepared containing 5.0 M NH$_4$OH in 100 mL deionized water. The reaction solution was prepared with 0.07 M H$_3$PO$_4$ and 0.07 M NH$_4$OH in 350 mL deionized water. The reaction solution was heated with stirring to ~80 °C, and the base and metal solutions were added dropwise at controlled rates to maintain a pH of ~8.5.

Nitrogen gas was bubbled through the solutions throughout the reaction to maintain inert atmosphere. The sample was recovered by filtration, washed, and dried before use.

In the next step, 10.62 g $NH_4Mn_{0.5}Fe_{0.5}PO_4 \cdot H_2O$ precursor was combined with 2.37 g Li_2CO_3, 0.11 g $CoC_2O_4 \cdot 2H_2O$, 0.19 g $MgC_2O_4 \cdot 2H_2O$, 0.22 g ANO, 0.33 g glucose, 0.55 g citric acid, 0.49 g $NH_4H_2PO_4$, and 14 g deionized water in an 80 mL ball mill jar with 60 g stainless steel milling media. The mixture was milled at 500 rpm for 6 h, yielding a homogeneous green paste. This was dried under vacuum at 80 °C for 6 h, ground to a fine powder, and calcined under Ar flow at 550 °C for 3 h.

The calcined product was then combined with 0.70 g lactose, 5 mg carboxymethylcellulose (CMC) dispersant, and ~15 g deionized water, and milled at 500 rpm for 1 h. The low-viscosity suspension was then pumped at 3 rpm into a Labfreez spray dryer. The spray drying temperature was set to 130 °C and a flow rate to 20 scfm, yielding an outlet temperature of ~64 °C and a pressure of 0.17 MPa. After spray drying, the product was calcined at 650 °C for 2 h under Ar flow to yield $LiMn_{0.5}Fe_{0.5}PO_4$ with the dopants incorporated, which is referred to as LMFP throughout the manuscript.

Electrochemical analyses

Cathode slurries were prepared by combining the cathode active material (CAM), Timcal C65 carbon black, vapor-grown carbon fiber (VGCF), and predissolved polyvinylidene fluoride (PVDF, Arkema) in weight ratios of 95 : 1.25 : 1.25 : 2.5 in an N-methyl pyrrolidone (NMP) based slurry. The mixture was agitated in multiple steps in a high-shear mixer (Thinky) at 2000 rpm before casting onto a carbon-coated Al current collector with a doctor blade to achieve a uniform thickness. The cathodes were dried in a 110 °C convection oven before transferring to a 110 °C vacuum oven, where they were stored until use. The cathode loading was ~4.8 mg cm^{-2} (~0.9 mA h cm^{-2}) for half-cells and ~18 mg cm^{-2} (~3.2 mA h cm^{-2}) for full-cells. All cathodes were calendered at 110 °C before use.

Graphite anode slurries were casted for full-cell tests. The slurry composition consisted of Imerys GHDR graphite, Timcal C65 carbon black, CMC, styrene butadiene rubber (SBR), and Soteras sodium lauryl sulfate dispersant in a 95 : 1 : 1.25 : 0.25 : 2.5 weight ratio, dispersed in water. 1.5 mg oxalic acid was added to the slurry to etch the copper foil current collector. The graphite slurries were casted to a thickness of ~4.0 mA h cm^{-2} to achieve an N/P ratio of ~1.15 when paired with the cathode. The graphite electrodes were dried in an 80 °C convection oven and calendered on room-temperature rollers.

Electrochemical measurements were carried out in half-cells and full-cells. Half-cells were constructed with a 450 μm thick Li metal counterelectrode, celgard 2325 polypropylene separator, and an electrolyte consisting of 1.0 M $LiPF_6$ in a solvent mixture of ethylene carbonate (EC) and ethyl methyl carbonate (EMC) in a 3 : 7 weight ratio. 2 wt% vinylene carbonate (VC) was added to aid in passivating the lithium–metal surface. Cathode discs for half-cells were punched to 12.7 mm diameter. For full-cells, 14.3 mm diameter cathode discs were

punched and matched with 15.8 mm anode discs. Two cells for each sample were tested to ensure reproducibility. All cells were assembled inside an argon-filled glovebox. Electrochemical tests were carried out on an Arbin BT2000 battery cycler or a Biologic VMP3 potentiostat.

Materials characterization

Scanning electron microscopy (SEM) and energy-dispersive X-ray spectroscopy (EDS) were carried out on a Tescan Vega SEM. The accelerating voltage was 10 kV. Cross-sectional samples of electrodes were prepared by cutting small areas from the casted electrodes and affixing them to a vertically-oriented SEM stub with double-sided adhesive carbon tape. Electrode powder samples were prepared by loading a small amount of each powder onto an SEM stub with carbon tape, and tapping the edges to achieve a thin, uniform sample layer. EDS analysis was performed with a Bruker EDS detector. X-ray diffraction (XRD) was carried out with a Rigaku Miniflex 600 benchtop XRD with a Cu Kα target (λ = 1.5406 Å). The powder samples were scanned from 2θ = 10°–80° with 2° min^{-1} scan speed. Inductively coupled plasma-optical emission spectroscopy (ICP-OES) analysis was carried out on an Agilent 5800 ICP instrument. Samples were prepared by recovering the separator discs from specified full-cells after cycling at 45 °C. The separator discs were treated with a solution of concentrated nitric and hydrochloric acid overnight, which was then diluted to 2 wt%. The diluted solution was analyzed with ICP, and multiple measurements across 4 distinct wavelengths were carried out to ensure reproducibility.

Results and discussion

Cathode design

Due to the susceptibility of layered oxide cathodes to oxygen loss and surface reconstruction at high operating voltages, surface coatings have been widely explored and demonstrated to effectively passivate against electrochemical degradation. Surface coating with Nb (i.e., $LiNbO_3$) has been extensively demonstrated,[27–29] serving to facilitate Li$^+$-ion conduction, while passivating the cathode material against irreversible electrochemical degradation. Consequently, we chose to incorporate a Nb coating (0.5 mol%) onto the $LiNi_{0.80}Mn_{0.10}Co_{0.10}O_2$ (NMC811) used in this work to optimize its electrochemical performance. Fig. S1 shows the X-ray diffraction (XRD) patterns of NMC811 and Nb@NMC811, confirming that no impurity phase is present and both materials match well with the $R\bar{3}m$ space group, characteristic of well-ordered layered oxides. Scanning electron microscopy (SEM) images were obtained to show the morphologies of the NMC811 and Nb@NMC811 (Fig. S2a and S2b), which consist of ~10 μm agglomerations of primary particles. Energy dispersive X-ray spectroscopy (EDS) confirms the presence of Nb in Nb@NMC811 (Fig. S2c and S2d).

The as-synthesized LMFP included trace amounts of Co (1 mol%), Mg (2 mol%), and Nb (1 mol%), with a nominal

composition of $LiMn_{0.5}Fe_{0.5}PO_4$. Cobalt is beneficial for improving bulk electronic conductivity due to enhanced bond covalency,[30] while Mg and Nb have been shown to enhance $Mn^{2+/3+}$ redox kinetics and interfacial Li^+ conductivity, respectively.[19] Fig. S3 shows the XRD pattern of the as-synthesized LMFP, which indexes well to the *Pnma* space group, confirming the olivine structure. The spray-drying method used during LMFP synthesis results in spherical secondary particles with ~5–10 μm diameter, as shown in Fig. S4.

The layered-olivine blended cathodes were prepared by mixing the as-synthesized Nb@NMC811 and LMFP in specified mass ratios during the cathode slurry preparation. Blended cathodes are referred to by the weight ratios of Nb@NMC811 and LMFP added to the slurry: the blend with 85% Nb@NMC811 and 15% LMFP is hereafter referred to as 85/15 Blend, and the blend with 70% Nb@NMC811 and 30% LMFP is hereafter referred to as 70/30 Blend. Cross-sectional SEM images of casted and calendared Nb@NMC811 and 70/30 Blend electrodes are shown in Fig. 1a and b. Fig. 1c and d show the corresponding EDS maps and spectra. The EDS data confirm the presence of Ni in both samples from the layered cathode constituent. For the 70/30 Blend cathode, the presence of P is also confirmed by the EDS data (Fig. 1d). The other elements identified include Al from the current collectors, C from the conductive carbon added to the cathode, F from the fluorinated binder, and O from both layered and olivine cathode constituents.

Ni and P were chosen for elemental mapping to represent, respectively, the regions of Nb@NMC811 and LMFP in each cathode. For the Nb@NMC811 cathode sample, the Ni map confirms that all the cathode particles are rich in Ni, while the weak signal in the P map is ascribed to baseline noise (Fig. 1c). For the 70/30 Blend sample, the Ni and P maps appear anticorrelated, confirming that particles of both Nb@NMC811 and LMFP constituents are evenly mixed, providing a macroscopically uniform cathode matrix.

Electrochemical characteristics of layered-olivine blended cathodes

NMC811 exhibits primarily solid-solution type behavior, with some first-order phase transitions (*e.g.*, H2–H3) appearing in certain SOC regimes.[31] This gives rise to continuously sloping voltage profiles, as shown in Fig. 2a. As Nb@NMC811 nears full lithiation during discharge (~3.6 V *vs.* Li/Li^+), the Li^+ diffusion coefficient drops significantly,[31] leading to dramatic impedance growth (Fig. 2b). Thus, the kinetic limitations of the layered oxide cathode induce severe polarization, causing the cell voltage to drop rapidly to the cutoff voltage (2.8 V *vs.* Li/Li^+) as discharge continues. This effect constrains the discharge capacity of layered oxide cathodes, particularly at medium or high rates.

LMFP undergoes (de)lithiation during both $Mn^{2+/3+}$ and $Fe^{2+/3+}$ redox. The predominantly 2-phase nature of these reactions yields flat voltage plateaus at ~4.1 V (corresponding to $Mn^{2+/3+}$) and 3.5 V ($Fe^{2+/3+}$) *vs.* Li/Li^+, as shown in Fig. 2a. The impedance data shown in Fig. 2c demonstrate that the impedance response of LMFP remains relatively stable throughout both voltage plateaus, manifesting more sluggish Li^+ diffusivity during the transition between the plateaus and as the cathode approaches very high or low SOC.

When LMFP is added to Nb@NMC811 to form the layered-olivine blended cathode, the resulting voltage profile exhibits features of both constituent cathodes, as shown by the profiles for the 85/15 Blend and 70/30 Blend cathodes in Fig. 2a. Notably, the $Fe^{2+/3+}$ plateau emerges as the impedance of the
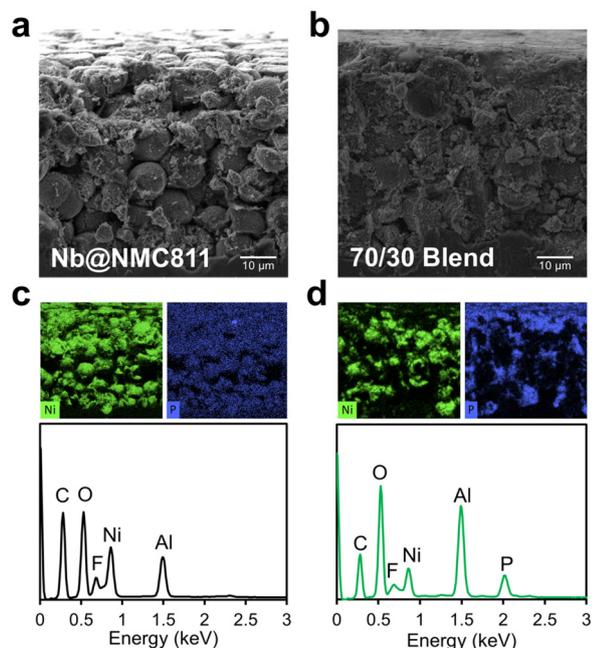
Fig. 1 Physical design of blended cathodes. Cross-sectional SEM images of (a) Nb@NMC811 and (b) 70/30 Blend cathodes. EDS maps and spectra of (c) Nb@NMC811 and (d) 70/30 blend cathodes.
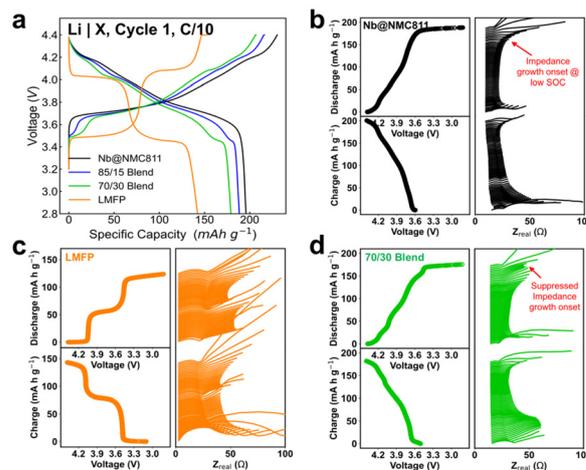
Fig. 2 Electrochemical Characteristics of Nb@NMC811–LMFP Blends. (a) Voltage profiles of cathode in half-cells with lithium−metal anode. GEIS data showing impedance evolution during (dis)charge for (b) Nb@NMC811, (c) LMFP, and (d) 70/30 Blend.

layered oxide component begins to rise, suppressing the impedance growth below 3.6 V due to parallel $Fe^{2+/3+}$ redox (Fig. 2d). This "buffer effect" has been identified before on blended cathode materials.[21,32–34] Specifically, the buffer effect refers to the increased contribution from the olivine cathode to the total current to compensate for the lower contribution from the layered cathode at <3.6 V, reducing voltage polarization.

This phenomenon enhances the discharge rate capability of layered-olivine blended cathodes in comparison to pure layered materials,[21,35] particularly at low SOC/voltage. Although Nb@NMC811 offers higher theoretical energy density than LMFP, the practical energy density depends strongly on operating conditions. Furthermore, the degree to which energy density is compromised by blending LMFP into Nb@NMC811 is dependent on operating conditions. Thus, we posit that it is possible to choose operating conditions for layered-olivine blends which take advantage of the buffer effect to reduce the energy density penalty, maximizing their benefits in comparison to pure layered-oxide cathodes. The next several sections are focused on exploring this hypothesis.
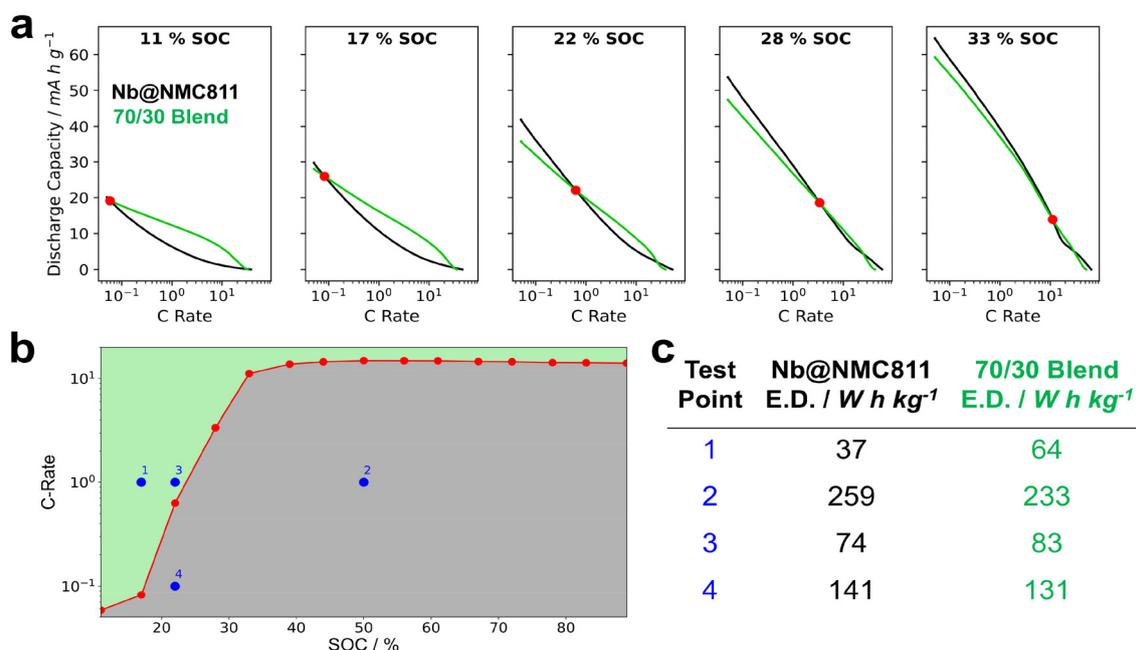
Critical rate analysis

Mapping the energy density for a broad range of SOC and C-rate conditions for multiple materials will be impractically exhaustive and may yield results of limited scope, which may not be transferrable to different materials and cell design parameters. Thus, we instead develop a method based on chronoamperometric rate testing, which can be rapidly implemented to compare the energy density of two cathodes based on the operating conditions. As shown in previous work, chronoamperometry can be applied to rapidly obtain a continuous rate performance profile for a cathode.[36] Thus, an SOC-dependent rate performance analysis can be carried out by charging cathodes to various SOCs and discharging at constant voltage. Because the cathodes are held at the same voltage throughout discharge, the measured capacity is directly proportional to the energy density.

An illustrative example is shown in Fig. 3. Nb@NMC811 and 70/30 blend cathodes were each assembled with a Li-metal anode in half-cells and formed at 18 mA g^{-1} at 2.8–4.4 V (Fig. S5), yielding, respectively, 196 and 180 mA h g^{-1} on first discharge. This discharge capacity was designated as 100% SOC for each respective cell. Then, each cell was charged at C/3 rate for times ranging from 20 min to 160 min, corresponding to, respectively, 11% SOC to 89% SOC. After each charge, the cell was discharged at constant voltage (2.80 V) until the current magnitude fell below a C/20 rate. The voltage *vs.* time profiles are given for Nb@NMC811 and 70/30 Blend in Fig. S6, showing the total test duration is ~35 h. From the chronoamperometry data during the potentiostatic discharge, the discharge capacity *versus* C-rate profiles were computed for each charge SOC. For simplicity, Fig. 3a shows these discharge profiles for 11%–33% SOC. The full sets of discharge profiles for each SOC are shown in Fig. S7.

Importantly, for each SOC, there exists an intersection point of the rate profiles, marked in red in Fig. 3a and S7. The C-rate values of the intersection points, together with the charge SOCs at which they are identified, are then used to construct the critical rate profile (CRP), shown in Fig. 3b. The CRP

Fig. 3 Overview of critical rate analysis for Nb@NMC811 *vs.* 70/30 Blend. (a) Constant-voltage discharge profiles for Nb@NMC811 and 70/30 blend after charging to various SOCs. (b) Critical rate profile (CRP) constructed from intersection points of discharge curves. (c) Table comparing the energy density of cathode materials for various operating conditions.

predicts the operating conditions (rate and SOC) for which both of the cathode materials compared offer equal energy density during a galvanostatic discharge to 2.80 V.

From the discharge profiles shown in Fig. 3a, it is also apparent that at C-rates higher than the intersection rate, the 70/30 Blend cathode delivers higher capacity than the pure Nb@NMC811 cathode. Although there does exist a second intersection point at very high rates (>20C), this occurs outside practical operating rate regimes and is attributed to differences in surface area between the porous electrodes. Consequently, it is predicted that within the operating region of the plot above the CRP, shaded in green (*i.e.*, for low SOC and high-rate operations), the 70/30 Blend cathode delivers higher energy density than the Nb@NMC811 cathode. Conversely, below the CRP, shaded in grey (for high SOC and low-rate operations), the Nb@NMC811 cathode delivers higher energy density.

The predictive accuracy of the CRA is verified by galvanostatic testing. Based on the CRP shown in Fig. 3b, four "test points", each corresponding to a certain SOC and discharge C-rate, were chosen for galvanostatic analysis. For clarity, the test points are also plotted and labeled on Fig. 3b. The cells were charged at C/3 rate for a certain time to reach the specified SOC, and then discharged at the specified C-rate. A table of results is provided in Fig. 3c. For each test point falling below the CRP (points 2 and 4), the Nb@NMC811 cathode delivers higher energy density than the blended cathode. For test points 1 and 3, which lie above the CRP, the blended cathode delivers higher energy density. This demonstrates that the CRA method accurately predicts the operating conditions under which a layered-olivine blended cathode will deliver higher energy density than the pure layered oxide cathode, and *vice versa*.

Notably, the CRA took less than two days to complete, whereas conventional galvanostatic rate-testing methods typically take weeks. The CRA portrays graphically the continuum of operating conditions under which the redox buffer effect may be exploited to deliver higher energy density. To the best of our knowledge, no previous study has quantified this phenomenon. Some general observations can be drawn from the CRP shown in Fig. 3b, which are developed below.

First, the critical C-rate is quite low at low SOCs. This suggests that at most practical C-rates under low SOC conditions (*e.g.*, <20% SOC), layered-olivine blend cathodes will deliver higher energy density than their pure layered oxide counterparts. This is consistent with our previous findings and highlights the excellent pulse-discharge performance of layered-olivine blends at low SOC.[21]

Second, at medium or high SOCs, the critical C-rate becomes quite high (>10C). It is reasonable to expect that at practical electrode loading conditions (*e.g.*, >3 mA h cm^{-2}), Li$^+$ diffusion limitations in the electrode pore structure would preclude the delivery of appreciable capacity at such rates. Thus, within most operating SOCs (>30%), a layered oxide cathode is expected to deliver higher energy density than a layered/olivine blend cathode due to the difference in theoretical energy densities.

Third, although the "Critical C-rate" defines the point at which the discharge profiles intersect, their values can be quite similar within a broader region especially at medium SOCs, as exemplified by the discharge curve from 33% SOC in Fig. S7. It will be shown later that this region of similarity is wider when comparing Nb@NMC811 to 85/15 Blend. Thus, for subsequent CRAs, we include a shaded region around the CRP representing a region of operating conditions, where the constant-voltage discharge capacities are within 1% of one another.

In consideration of the above observations, we can propose that the most viable use cases for layered-olivine blends are characterized by (i) low critical C-rate over a broad range of SOCs and (ii) similar capacity over a broad range of C-rates at high SOCs. Therefore, we chose to further investigate the effects of niobium coating, blend ratio, and operating temperature on the CRP.

Effect of niobium content

In general, the niobium coating on layered oxide cathodes improves interfacial charge-transfer kinetics and shields the cathode material against parasitic side reactions leading to capacity loss.[27,28,37] In the case of Nb-coated NMC811, this results in higher capacity and more stable cycling. Fig. 4 provides a comparison of NMC811 and Nb@NMC811. The two materials were initially compared in half-cells, with lithium–
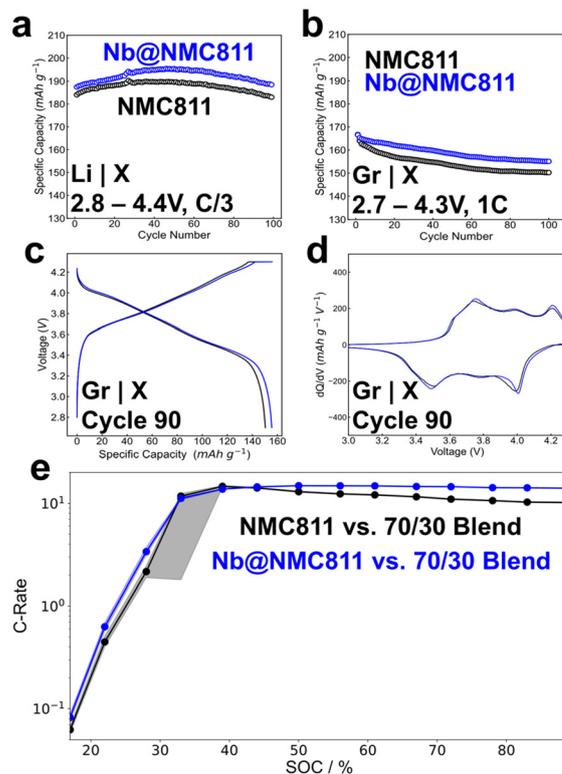
Fig. 4 Effect of Nb coating on NMC811. Cycling performances of NMC811 and Nb@NMC811 in (a) half-cells and (b) full-cells. (c) Voltage profiles and (d) d*Q*/d*V* profiles showing how Nb coating improves discharge capacity and structural stability of NMC811. (e) CRPs of NMC811 and Nb@NMC811 compared to 70/30 Blend.

metal anodes, as shown in Fig. 4a. Nb@NMC811 delivers ~5 mA h g^{-1} higher discharge capacity than NMC811 at C/3 rate. After ~60 cycles, both samples experience capacity fade at a similar rate, which is attributed to the precipitous rise seen in half-cell impedance, correlated with parasitic side reactions at the lithium–metal anode.[38]

To test the materials in a more realistic cell format, coin full-cells with a graphite anode were tested for each cathode. As shown in Fig. 4b, the full-cells exhibit a capacity difference similar to the half-cells, but are more stable in extended cycling. The higher capacity of Nb@NMC811 in full-cells can be attributed to the role of the niobium coating in reducing surface reconstruction and impedance growth.[28] This manifests as lower (dis)charge overpotential, as shown by the voltage profiles in Fig. 4c. Fig. 4d presents the dQ/dV analyses for each material, showing the lower voltage hysteresis exhibited by Nb@NMC811. Moreover, the more pronounced peaks corresponding to the H2–H3 phase transitions in Nb@NMC811 at high SOC confirm that the niobium coating improves the high-voltage stability of the cathode.

Finally, CRAs were carried out as described above to compare NMC811 to 70/30 Blend and Nb@NMC811 to 70/30 Blend. The resulting CRPs are shown in Fig. 4e. In the case of the Nb@NMC811, the CRP is generally higher than that for the bare NMC811 comparison, indicating that the point of

intersection between the discharge profiles is observed at a higher C-rate, as shown by the discharge profiles in Fig. S8. This is consistent with expectations, as the superior electrochemical kinetics of Nb@NMC811 compared to NMC811 yield higher energy density than the blended cathode material over a broader range of operating conditions. In consideration of this result, we chose to focus on comparing Nb@NMC811 to 85/15 Blend and 70/30 Blend for the subsequent analyses.

Effects of blend ratio and operating temperature

It is expected that the CRP depends significantly on the blending ratio between layered and olivine constituents. As the buffer effect of Fe$^{2+/3+}$ redox becomes more prominent with increasing proportion of LMFP, the discharge rate capability from low SOC is continuously improved, as exemplified in Fig. S9–S11 for low (<30%) SOC tests across three different operating temperatures. However, this benefit comes at the expense of discharge capacity from higher SOC, such that the 70/30 Blend delivers significantly lower discharge capacity than the 85/15 Blend and Nb@NMC811.

In the CRP, this phenomenon manifests as an SOC-dependent comparison between the two blend ratios: at low SOC, the critical rate is lower for the blend with higher LMFP content, whereas at medium or high SOC, the opposite is true. This behavior is shown for various temperatures in Fig. 5a–c.
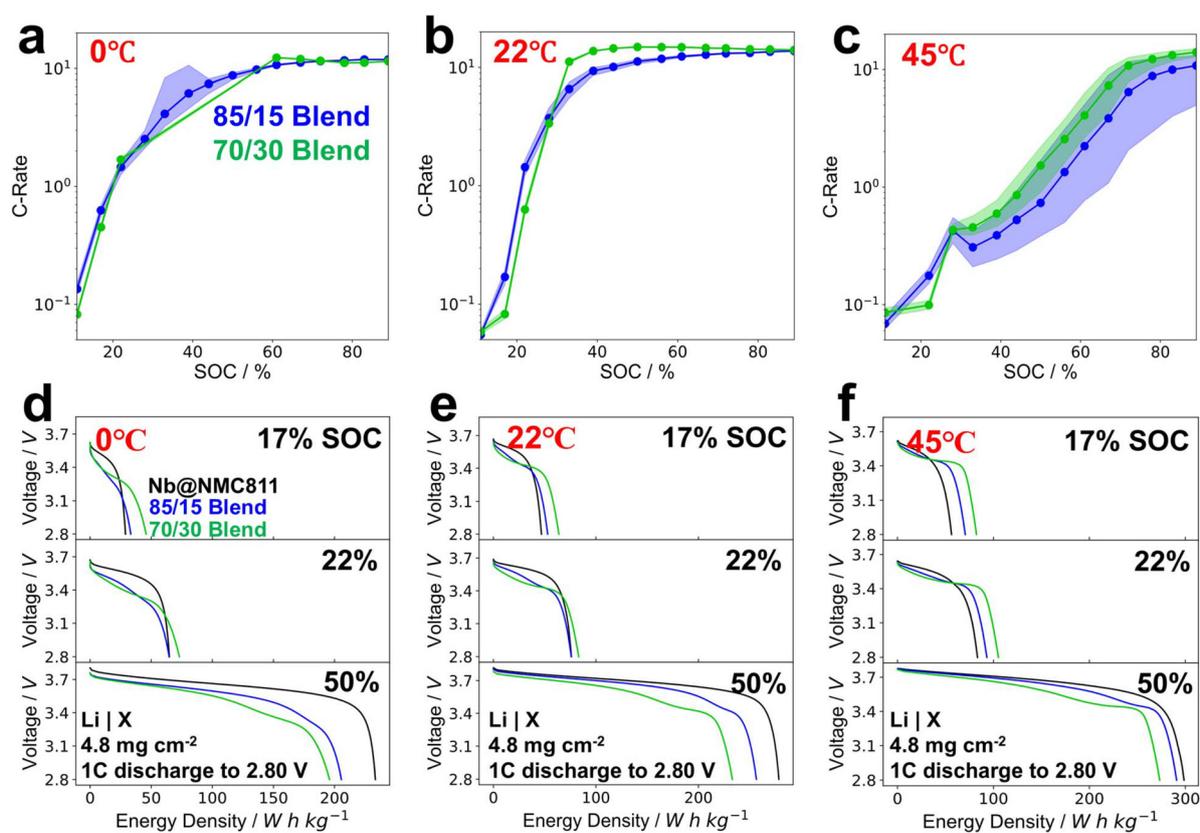

Fig. 5 Application of CRA for different temperatures and blend ratios in half-cells. CRPs comparing Nb@NMC811 to 85/15 Blend and 70/30 Blend at (a) 0 °C, (b) 22 °C, and (c) 45 °C. 1C rate galvanostatic discharge tests after charging to various SOCs, at (d) 0 °C, (e) 22 °C, and (f) 45 °C.

Additionally, the shaded region indicating ≤1% difference is significantly broader for the blend with lower LMFP content, indicating a broader range of operating conditions in which the energy density is expected to be similar for the blended cathode and the pure layered oxide cathode.

Changes in operating temperature can have dramatic effects on the electrochemical and transport kinetics taking place in electrodes, significantly affecting their energy densities. In the case of blended electrodes, these phenomena may manifest to a different degree in each constituent material, further complicating the prediction of their response to temperature changes. Thus, it is valuable to extend our analyses to evaluate the impacts of varied operating temperatures on the performance of blended cathodes.

By comparing the CRPs at different temperatures, a clear trend emerges. As the temperature increases from 0 °C to 45 °C, the CRPs shift toward lower rates/higher SOCs (Fig. 5a–c). This shift is especially pronounced at 45 °C, where the CRPs are shifted down significantly at SOCs up to ~60% (Fig. 5c). Therefore, at elevated temperatures, there is a wider region of operating conditions within which 85/15 Blend and 70/30 Blend are predicted to deliver higher energy density than Nb@NMC811. More generally, the energy density penalty associated with blending LMFP into layered oxides is reduced at higher temperatures.

To confirm the CRA predictions, galvanostatic discharge tests were carried out at 1C rate for 17%, 22%, and 50% SOCs at each temperature, shown in Fig. 5d–f. At each temperature, the energy density delivered by the 85/15 Blend and 70/30 Blend cathodes is overtaken by the Nb@NMC811 as the SOC increases from 17% to 50%. However, this effect is minimized as the temperature increases. At 45 °C, the 85/15 Blend and 70/30 Blend cathodes deliver significantly higher energy density at 22% SOC than Nb@NMC811, and the difference in energy density delivered at 50% SOC is significantly smaller than at lower temperatures (Fig. 5d). These results confirm that layered-olivine blends offer the most competitive energy density at elevated temperatures, and at low SOCs.

Two key conclusions may be drawn from this analysis. First, high-temperature, high-rate, and low-SOC operations are optimal for maximizing the energy density of layered-olivine blends in comparison to pure layered oxide cathodes. Second, increasing the content of LMFP in the blended cathode yields significantly higher capacity at low SOC, but incurs a larger loss of available energy density at high SOCs.

After the CRA and galvanostatic discharge tests, the half-cells were subjected to 100 cycles at the same temperatures used for CRA tests. The rate was 60 mA g^{-1} or approximately C/3. The resulting half-cell tests at each temperature are shown in Fig. 6. As expected, as the temperature is increased from 0 °C to 45 °C, the capacity of each electrode composition increases significantly due to more facile Li$^+$-transport kinetics.

At 0 °C, the capacity of each cell remains quite stable throughout the cycling tests, as the kinetic limitations arising from the low temperature mask progressive irreversible capacity loss (Fig. 6a). At 22 °C, the capacities remain fairly stable across all samples, but begin to decrease at the same rate after 60 cycles. Due to the intrinsic stability of olivine-phase LMFP, this continuous capacity loss is attributed to the increasing polarization of the lithium–metal anode, which is well-known to limit the cycle life of half-cells.[38]

At 45 °C, all cells experience more rapid capacity fade compared to lower temperatures, which is attributed to the accelerated rate of parasitic side reactions with the lithium–metal anode.[39] Notably, however, the rate of fade for the blended cathodes is significantly suppressed compared to the Nb@NMC811 at high temperature. The improved stability of blended cathodes at high temperature is attributed to the excellent electrochemical stability of the LMFP constituent, and is corroborated by previous data.[26] Notably, however, LMFP suffers from Mn dissolution at high temperature, which can lead to loss of capacity.[17,40] We speculate that the inferior stability of 70/30 Blend compared to 85/15 Blend results from more significant capacity fade from the LMFP component.

The coulombic efficiencies (CE) corresponding to each of the tests shown in Fig. 6 are shown in Fig. S12. The average CE
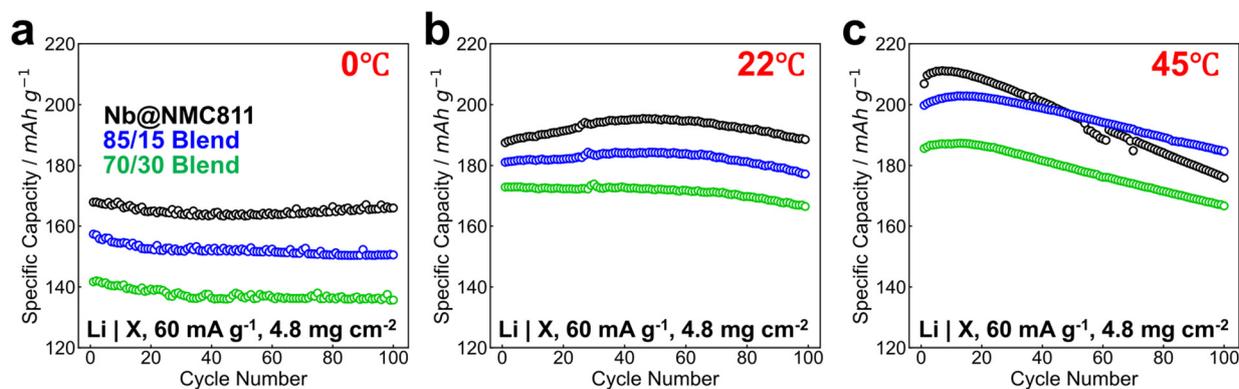

Fig. 6 Cycling performances of Nb@NMC811, 85/15 Blend, and 70/30 Blend in half-cells with lithium−metal anode at (a) 0 °C, (b) 22 °C, and (c) 45 °C.

values are indicated in each plot. For each cathode, the CE increases continuously with operating temperature. Notably, however, the CE values of the blended cathodes tend to increase more significantly with temperature than those of the Nb@NMC811 cathode, highlighting the superior high-temperature stability of the blended cathodes.

Fig. S13 compares the C/10 voltage profiles before and after the cycling tests shown in Fig. 6 in order to compare the irreversible capacity loss incurred during the cycling test. At 0 °C, slight increases in polarization are observed for each material on discharge, leading to slightly lower reversible capacity after 100 cycles (Fig. S13a). Very similar behavior is observed at 22 °C (Fig. S13b), although significantly lower voltage is observed after cycling during the 70/30 Blend cathode discharge, which appears to originate from a loss of capacity in the $Mn^{2+/3+}$ plateau of LMFP. At 45 °C, significant irreversible capacity loss is observed for all materials (Fig. S13c). This effect is most prominent for Nb@NMC811, which exhibits voltage fade characteristic of active material loss.[41] Similar to the results shown in Fig. 6, the irreversible capacity loss is suppressed for both the blended cathodes, but slightly more for the 85/15 Blend than for the 70/30 Blend.

These tests demonstrate that the blended cathodes offer the best performance compared to Nb@NMC811 at elevated operating temperature. At 45 °C, the balance between energy density and cycle life is most favorable for the blended cathodes. With these considerations, we proceed to investigate how elevated temperature affects the energy density of lithium-ion full cells at various rates.

Performance and relative cost comparison of layered-olivine blends in full cells

To prepare full-cells, cathodes with an active material loading of ~18 mg cm^{-2} (~3.2 mA h cm^{-2}) were prepared, and the graphite anodes were prepared with a loading to maintain an N/P ratio of ~1.15. The coin-type full-cells were subjected to three cycles at C/10 rate, at ambient temperature (22 °C) or 45 °C. Whereas the previous tests considered the performance of each material for a range of SOCs, these tests address the behavior when discharging from a fully charged state with a more practical cell design. Consequently, after the formation cycles, the cells were charged galvanostatically to 4.3 V and held at 4.3 V until the current dropped below C/20, before discharging at various rates. Fig. 7 compares the full-cell test results for each cathode composition across various discharge rates and temperatures.

We first compare the rate capabilities of full-cells of each material at 22 °C (Fig. 7a) and 45 °C (Fig. 7b). At lower C-rates, Nb@NMC811 offers higher energy density than the blended cathodes. However, at higher C-rates, the energy density penalty of the blended cathodes is minimized. When comparing the results between 22 °C and 45 °C, the rate capability of all cathode materials improves with temperature. In particular, the 85/15 Blend offers similar energy density to Nb@NMC811 at 45 °C as the rate is increased, virtually eliminating the energy density penalty observed at 22 °C.
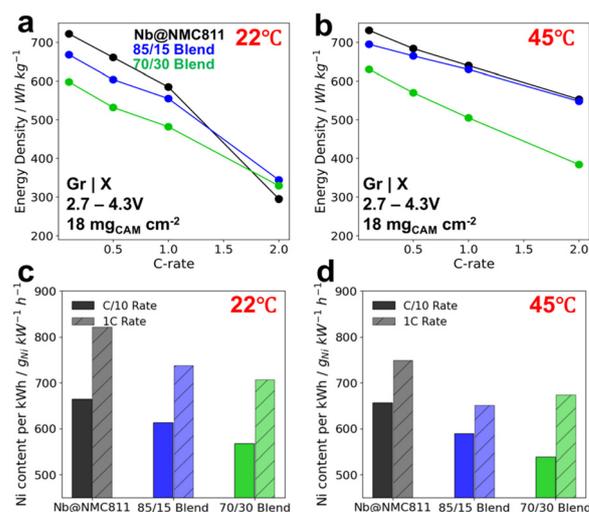

Fig. 7 Rate performances and relative cost analysis for layered-olivine blends under various operating conditions in full-cells. Rate capability of layered-olivine blends at (a) 22 °C and (b) 45 °C. Cost comparison based on nickel content per kWh for each cathode at C/10 and 1C discharge rates at (c) 22 °C and (d) 45 °C.

Although these results corroborate the earlier findings, which predicted that the blended cathodes would offer more competitive energy density compared to Nb@NMC811 at higher rates and temperatures, they do not entirely reflect the predictions of the CRA. Specifically, the 85/15 Blend cathode offers more competitive performance in comparison to the Nb@NMC811 cathode than was predicted by the earlier CRA results, delivering similar energy density (<2% difference) even at full SOC, at a 1C rate. This suggests that in full-cells under practical loading and moderate or high rate conditions, layered-olivine blended cathodes may offer energy density more comparable to that of layered oxide cathodes. Fig. S14 compares the voltage profiles between 22 °C and 45 °C for C/10 and 1C rates, showing the difference in voltage polarization for each material under different conditions. The difference in voltage polarization in blended cathodes compared to Nb@NMC811 may be partially attributed to parallelization of the current load across both electrode components.[42] Notably, the capacity of the 70/30 Blend cathode is significantly lower than that of the 85/15 Blend or Nb@NMC811 at 45 °C, which may be due to the effects of Mn dissolution. ICP-OES results are shown in Fig. S15 to confirm that 70/30 Blend experiences significant Mn dissolution at elevated temperatures compared to Nb@NMC811.

It is important to consider that the density of the cathode decreases monotonically with increasing LMFP content. For Nb@NMC811, 85/15 Blend, and 70/30 Blend, the electrode press densities were, respectively, 3.60 g cm^{-3}, 3.26 g cm^{-3}, and 2.93 g cm^{-3}. As the electrode press density decreases, it is expected that decreasing pore resistance also plays a significant role in the superior rate capability of blended cathodes.[43] Because pore resistance is a much less significant source of

impedance under low loading conditions, this effect is less apparent in the half-cell tests above.

Furthermore, due to the different density between electrodes, the volumetric energy density trends differently from the gravimetric energy density shown in Fig. 7a and b. To address this, Fig. S16a and S16b present the volumetric energy density (VED) of each electrode for the same rate and temperature conditions. Evidently, Nb@NMC811 offers significantly higher VED than the blended cathodes due to its higher press density. However, owing to the superior rate capability of the blended cathodes, the trends with increasing rate and temperature remain the same as in the comparison of gravimetric energy density.

Beyond performance, a major motivation driving interest in layered-olivine blended cathodes is their reduced cost, as addressed in our previous work.[21] It is difficult to accurately predict the cost of the cathode compositions studied herein, as estimates of material and processing costs vary widely.[21,44,45] However, it is well established that the nickel content in NMC811 is the most costly part of the cathode,[9,46] which is also true in the blended cathodes studied here. By weight, nickel represents 48% of Nb@NMC811, 41% of 85/15 Blend, and 34% of 70/30 Blend cathode materials. Therefore, we use nickel mass per unit energy as a basis to compare the cathode cost in full-cells at C/10 and 1C rates.

In Fig. 7c and d, this comparison is presented for operating temperatures of, respectively, 22 °C and 45 °C. Despite the lower energy density of blended cathodes at slow rates, the significant reduction in nickel content still yields an overall reduction in g_{Ni} kW^{-1} h^{-1} for the blended cathodes compared to Nb@NMC811. At 22 °C, this trend is directly related to the LMFP content of the cathode at both C/10 and 1C rates (Fig. 7c). At 45 °C and 1C rate, the g_{Ni} kW^{-1} h^{-1} reaches a minimum for 85/15 Blend, which is 13% lower than that for Nb@NMC811 (compared to 10% at 22 °C), and 4% lower than that for 70/30 Blend (Fig. 7d). These data indicate that operating at elevated temperature and high rates maximizes the cost benefit of layered-olivine blends. However, blending in excessive LMFP does not necessarily lead to further reduction in cost per kWh, due to the significant reduction in energy density.

Blending layered and olivine cathodes has been identified as a compelling strategy for developing lower-cost LIBs. In general, it is inferred that blending olivine cathodes into layered oxides will reduce the cost per unit energy and improve cycling stability, but also reduce the energy density of the cathode due to the differences in theoretical energy density between the two cathode materials. However, as we have shown herein, this assumption neglects the differences in electrochemical kinetics, which arise due to different operating voltages.

Due to the enhanced electrochemical kinetics at low voltage, layered-olivine blends can exhibit enhanced rate capability compared to pure layered oxide cathodes. Consequently, at high rates, they can deliver energy density similar to their pure layered oxide counterparts. This observation offers profound insights into the design of blended cathodes to satisfy different use cases.

In general, the approach of blending two distinct cathode materials raises many considerations, and much remains to be understood about layered-olivine blends in particular. The CRA technique may be employed to understand how the SOC-dependent rate capability depends on various parameters, such as materials aging, electrode loading, and relative morphology of the layered and olivine component particles. The improvement in kinetics, which is inherent of blended cathode materials, suggests that incorporation of Nb-incorporated high-Mn LMFP to increase the theoretical energy density of LMFP also merits pursuit.[19,42]

Testing of blended electrodes under more practical electrode loading conditions is often overlooked in the literature. However, as demonstrated in this work, this offers valuable insights which can be masked when only comparing electrodes under low loading conditions and in half-cells. To benefit their practical application, it is critical that future work addresses in greater detail the effects of electrode loading, N/P ratio, and electrode press density on the behavior of layered-olivine blend electrodes in extended cycling tests.

It is further noted that the constant-voltage discharge curves shown throughout the manuscript (e.g., Fig. 3a, Fig. S9–S11) display distinct multicomponent trends at high C-rates as the LMFP content is increased. While beyond the scope of the present study, rigorous impedance analyses of blended electrodes, and in particular layered-olivine blends, is a highly worthwhile direction for future study. By constructing an equivalent-circuit model that adequately describes blended electrode systems, a quantitative model predicting their rate-dependent behavior may be developed, as shown previously for pure electrodes.[36]

Conclusions

In this study, we have evaluated the electrochemical performance of Nb@NMC811–LMFP cathode blends compared to pure Nb@NMC811. We developed the critical rate analysis (CRA) technique to rapidly and comprehensively determine the operating conditions for which each cathode will offer more favorable energy density. This analysis allows us to generally conclude that Nb@NMC811–LMFP blends offer their most competitive performance at elevated temperatures and high C-rates. Our full-cell tests demonstrate that this principle holds true under more practical cell design conditions: at elevated temperature and high rate conditions, Nb@NMC811–LMFP blends can offer higher energy density, which translates to a more significant reduction in cost per kWh. Finally, the proportion of LMFP added to the Nb@NMC811 must be carefully chosen to balance these benefits with the energy density penalty incurred under less favorable operating conditions. We believe these analytical techniques and findings will be of great value to the continued development and application of blended cathode materials.

Author contributions

S. O. developed the project idea and methodology, and carried out all experimental analyses. A. M. supervised the research.

Conflicts of interest

There are no conflicts to declare.

Data availability

All the data associated with the findings presented in this study are available within this article and its SI.

Supplementary information is available, including preliminary XRD and SEM data, rate profiles, voltage profiles, and ICP data. See DOI: https://doi.org/10.1039/d5eb00132c.

Acknowledgements

References

1 A. Manthiram, *Nat. Commun.*, 2020, **11**, 1–9.

2 W. Lee, S. Muhammad, C. Sergey, H. Lee, J. Yoon, Y.-M. Kang and W.-S. Yoon, *Angew. Chem., Int. Ed.*, 2020, **59**, 2578–2605.

3 C. Heubner, T. Liebmann, M. Schneider and A. Michaelis, *Electrochim. Acta*, 2018, **269**, 745–760.

4 S. B. Chikkannanavar, D. M. Bernardi and L. Liu, *J. Power Sources*, 2014, **248**, 91–100.

5 D. Chatzogiannakis, O. Arcelus, E. Ayerbe, P. Ghorbanzade, B. Ricci, I. de Meatza and M. R. Palacin, *Soc. Sci. Res. Network*, 2025, **428**, 116942.

6 International Energy Agency, Trends in electric vehicle batteries – Global EV Outlook 2024, https://www.iea.org/reports/global-ev-outlook-2024/trends-in-electric-vehicle-batteries, (accessed 3 May 2025).

7 J. Zhao, Lithium Manganese Iron Phosphate (LMFP) Batteries Receiving Renewed Attention In China — Expected To Be Installed Mainly In Middle-Class EVs, Mitsui Co. Global Strategic Studies Institute, 2023.

8 M. Jiang, D. L. Danilov, R.-A. Eichel and P. H. L. Notten, *Adv. Energy Mater.*, 2021, **11**, 2103005.

9 J.-J. Marie and S. Gifford, Developments in Lithium-Ion Battery Cathodes, The Faraday Institution, 2023.

10 S. Ma, X. Zhang, S. Wu, E. Fan, J. Lin, R. Chen, F. Wu and L. Li, *Energy Storage Mater.*, 2023, **55**, 556–565.

11 S. Lee, L. Su, A. Mesnier, Z. Cui and A. Manthiram, *Joule*, 2023, **7**, 2430–2444.

12 J. B. Adamo and A. Manthiram, *ACS Appl. Energy Mater.*, 2025, **8**, 2200–2208.

13 G. Bree, J. Zhao, V. Majherova, D. Proprentner, G. J. Paez Fajardo and L. F. J. Piper, *Energy Fuels*, 2025, **39**, 3683–3689.

14 J. Liu, Y. Wu, B. Zhang, X. Xiao, Q. Hu, Q. Han, L. Wang, F. Bei and X. He, *Small*, 2024, **20**, 2309629.

15 S. Li, H. Zhang, Y. Liu, L. Wang and X. He, *Adv. Funct. Mater.*, 2024, **34**, 2310057.

16 S. Reed, K. Scanlan and A. Manthiram, *J. Mater. Chem. A*, 2024, **12**, 21341–21349.

17 K. Leslie, J. Harlow, D. Rathore, K. Tuul and M. Metzger, *J. Electrochem. Soc.*, 2024, **171**, 040520.

18 I. A. Shkrob, A. J. Kropf, T. W. Marin, Y. Li, O. G. Poluektov, J. Niklas and D. P. Abraham, *J. Phys. Chem. C*, 2014, **118**, 24335–24348.

19 P. Vanaphuti and A. Manthiram, *Small*, 2024, **20**, 2404878.

20 Shanghai Metal Market.

21 S. Lee, K. Scanlan, S. Reed and A. Manthiram, *Adv. Energy Mater.*, 2024, **15**(5), 2403002.

22 B. Zhang, X. Xie, Z. Peng, G. Hu, K. Du, B. Makuza, Y. Gong, X. Ji and Y. Cao, *J. Power Sources*, 2022, **541**, 231671.

23 C.-S. Kim, K. Kim, A.-S. Im, S.-S. Kim, J. Kim and J.-Y. Eom, *Electron. Mater. Lett.*, 2024, **20**, 799–806.

24 Z. Zhang, T. Liu, C. Gao, Y. Liu, H. Kuai, H. Du, W. You, X. Huang, J. Shen, H. Huang, Y. Su and L. Chen, *J. Energy Chem.*, 2024, **99**, 580–592.

25 J. Liu, J. Dong, M. Wang, N. Liu, H. Wang, K. Yan, H. Zhang, X. Wang, R. Tang, Y. Lu, Q. Qi, Y. Su, F. Wu and L. Chen, *eTransportation*, 2025, 100428.

26 Y. Yan, Y. Zheng, H. Zhang, J. Chen, G. Zeng, L. Wang, B. Zhang, S. Zhou, Y. Tang, A. Fu, L. Zheng, H. Huang, Y. Zou, C.-W. Wang, X. Kuai, Y. Sun, Y. Qiao and S.-G. Sun, *Adv. Funct. Mater.*, 2023, **33**, 2304496.

27 T. J. Watts and A. Manthiram, *J. Mater. Chem. A*, 2024, **12**, 29998–30011.

28 S. Ober, A. Mesnier and A. Manthiram, *ACS Appl. Mater. Interfaces*, 2023, **15**, 1442–1451.

29 F. Xin, H. Zhou, Y. Zong, M. Zuba, Y. Chen, N. A. Chernova, J. Bai, B. Pei, A. Goel, J. Rana, F. Wang, K. An, L. F. J. Piper, G. Zhou and M. S. Whittingham, *ACS Energy Lett.*, 2021, **6**, 1377–1382.

30 H. Gao, L. Jiao, J. Yang, Z. Qi, Y. Wang and H. Yuan, *Electrochim. Acta*, 2013, **97**, 143–149.

31 K. Märker, P. J. Reeves, C. Xu, K. J. Griffith and C. P. Grey, *Chem. Mater.*, 2019, **31**, 2545–2554.

32 C. Heubner, T. Liebmann, C. Lämmel, M. Schneider and A. Michaelis, *J. Energy Storage*, 2018, **20**, 101–108.

33 D. Chatzogiannakis, V. Arszelewska, P.-E. Cabelguen, F. Fauth, M. Casas-Cabanas and M. R. Palacin, *Energy Storage Mater.*, 2024, **69**, 103414.

34 D. Chatzogiannakis, M. Palacin and M. Casas-Cabanas, *ECS Meeting Abstracts*, 2023, MA2023-02, 223.

35 K. G. Gallagher, S.-H. Kang, S. U. Park and S. Y. Han, *J. Power Sources*, 2011, **196**, 9702–9707.

36 R. Tian, P. J. King, J. Coelho, S.-H. Park, D. V. Horvath, V. Nicolosi, C. O'Dwyer and J. N. Coleman, *J. Power Sources*, 2020, **468**, 228220.

37 J. Ren, Z. Liu, Y. Tang, Z. Yin, T. Yang, Z. Huang, W. Wang, W. Cui, C. Zhang, Z. Shen, Y. Liu, Y. Ren and Q. Liu, *J. Power Sources*, 2024, **606**, 234522.

38 R. C. McNulty, E. Hampson, L. N. Cutler, C. P. Grey, W. M. Dose and L. R. Johnson, *J. Mater. Chem. A*, 2023, **11**, 18302–18312.

39 J. Zheng, M. H. Engelhard, D. Mei, S. Jiao, B. J. Polzin, J.-G. Zhang and W. Xu, *Nat. Energy*, 2017, **2**, 17012.

40 M. Saulnier, A. Auclair, G. Liang and S. B. Schougaard, *Solid State Ionics*, 2016, **294**, 1–5.

41 W. Li, X. Liu, Q. Xie, Y. You, M. Chi and A. Manthiram, *Chem. Mater.*, 2020, **32**, 7796–7804.

42 C. Heubner, T. Liebmann, C. Lämmel, M. Schneider and A. Michaelis, *Batteries Supercaps*, 2022, **5**, e202100171.

43 R. Morasch, J. Keilhofer, H. A. Gasteiger and B. Suthar, *J. Electrochem. Soc.*, 2021, **168**, 080519.

44 M. Wentker, M. Greenwood and J. Leker, *Energies*, 2019, **12**, 504.

45 S. Ahmed, S. E. Trask, D. W. Dees, P. A. Nelson, W. Lu, A. R. Dunlop, B. J. Polzin and A. N. Jansen, *J. Power Sources*, 2018, **403**, 56–65.

46 W. Li, E. M. Erickson and A. Manthiram, *Nat. Energy*, 2020, **5**, 26–34.